

LETTER TO THE EDITOR

# Water-Cooled (sub)-Neptunes Get Better Gas Mileage

Tatsuya Yoshida<sup>1</sup> and Eric Gaidos<sup>2,3</sup>

<sup>1</sup> Faculty of Science, Tohoku University, Sendai, Miyagi 980-8578, Japan  
e-mail: tatsuya@tohoku.ac.jp

<sup>2</sup> Department of Earth Sciences, University of Hawai'i at Mānoa, Honolulu, Hawai'i 96822 USA e-mail: gaidos@hawaii.edu

<sup>3</sup> Institute for Astrophysics, University of Vienna, 1180 Vienna, Austria

Received September 30, 20XX

## ABSTRACT

The demographics of sub-Jovian planets around low-mass stars is dominated by populations of “sub-Neptunes” and “super-Earths”, distinguished by the presence or absence of envelopes of low-molecular weight volatiles, i.e., H<sub>2</sub>, He, and H<sub>2</sub>O. The current paradigm is that sub-Neptunes on close-in orbits evolve into super-Earths via atmospheric escape driven by high-energy stellar irradiation. We use an integrated hydrodynamic-radiation-chemical network model of outflow to demonstrate that this escape is modulated by the abundance of H<sub>2</sub>O, an efficient infrared coolant. Increasing H<sub>2</sub>O/H<sub>2</sub> at the base of the flow induces an order-of-magnitude decline in escape rate, with definitive consequences for retention of envelopes over Gyr. We show that saturation limits on H<sub>2</sub>O in the upper atmospheres of temperate sub-Neptunes could explain the paradoxical observations that these objects disappear more rapidly than their counterparts closer to their host stars. We also propose that the scarcity of sub-Neptunes around very low mass stars could be related to the water-poor chemistry of their antecedent protoplanetary disks. Observations of atmospheric H<sub>2</sub>O by *JWST* as well as searches for atmospheric escape from younger planets using H and He lines could test these predictions.

**Key words.** Planets and satellites: atmospheres — Planets and satellites: physical evolution — Planet-star interactions

## 1. Introduction

A photometric survey for transiting exoplanets by *Kepler* showed that Earth- to Neptune-size planets are far more numerous on close-in orbits around solar-type stars than Jovian counterparts (Howard et al. 2012; Petigura et al. 2013). Spectroscopic refinement of host star (and hence transiting planet) radii confirmed that this population consists of distinct “super-Earth” and “sub-Neptune” moieties with modal radii of about 1.3 and 2.2 $R_{\oplus}$  separated by a sparsely-populated valley at  $\sim 1.7R_{\oplus}$  (Owen & Wu 2013; Fulton et al. 2017; Petigura et al. 2022). This distribution appears to be universal among low-mass stars including M dwarfs (Cloutier & Menou 2020; Hirano et al. 2021; Venturini et al. 2024; Gaidos et al. 2024).

Planets much larger than the Earth but smaller than Neptune have no Solar System analog and their formation, composition, and evolution are active areas of investigation in exoplanet research. Available combinations of both mass and radius measurements indicate that super-Earths are primarily rocky while sub-Neptunes have thick, low-density envelopes comprised of low molecular weight molecules, particularly H<sub>2</sub>/He or H<sub>2</sub>O, around a rocky/icy core (Weiss & Marcy 2014). In the current paradigm, sub-Neptunes can lose their envelopes and evolve into super-Earths, and there is at least tentative evidence for atmospheric escape from some objects (e.g., Gaidos et al. 2022; Zhang et al. 2023; Rockcliffe et al. 2023; Orell-Miquel et al. 2023; Masson et al. 2024).

Photoevaporation of a planetary atmosphere occurs when its upper layers are heated by stellar extreme ultraviolet (EUV) ra-

diation<sup>1</sup> to the energies required for escape. Under sufficiently high irradiation, a collisional hydrodynamic flow can develop. The temperature profile in such a flow is governed by a balance between absorption of stellar EUV radiation vs. work done by the outflow, plus radiative cooling by atmospheric components. Radiative cooling is usually inefficient because absorption of X-rays and EUV invariably occurs above the homopause (or turbopause) where eddy diffusion can transport molecules against gravitational segregation. On Earth, the most important coolant molecules are CO<sub>2</sub> and, more variably, nitric oxide (NO, Kockarts 1980). High levels of CO<sub>2</sub> in the Archaean terrestrial atmosphere would have caused dramatically reduced upper atmosphere temperatures relative to the present, suppressing escape (Johnstone et al. 2018). Recent anthropogenic increase in CO<sub>2</sub> has caused a small but measurable decline in mesosphere/lower thermosphere temperatures (Roble & Dickinson 1989; Mlynczak et al. 2022).

H<sub>2</sub>O has a lower molecular weight and is a more effective IR radiator than either CO<sub>2</sub> or NO, but on Earth, with an equilibrium temperature  $T_e \approx 255$  K, H<sub>2</sub>O is trapped in oceans and by condensation at altitudes  $\lesssim 15$  km, far below the homopause at 90 km. On planets with higher equilibrium temperatures, especially those in a “runaway” greenhouse state, H<sub>2</sub>O is entirely in the atmosphere (Kasting 1988) and the Clausius-Clapeyron relation permits higher H<sub>2</sub>O in the upper atmosphere. In sub-Neptunes with envelopes of H<sub>2</sub>-He, super-runaway irradiation means that interior H<sub>2</sub>O is in a supercritical phase that could be miscible with H<sub>2</sub>, allowing it to mix throughout the convective atmosphere (Pierrehumbert 2023). Planets with inflated, steam-

<sup>1</sup> X-rays and far-UV radiation make only minor contributions to heating (e.g., Owen et al. 2020).

dominated atmospheres could be present in or even dominate the small planet population on close-in orbits (Turbet et al. 2020; Piaulet-Ghorayeb et al. 2024). On the other hand, some planets may have accreted from oxygen-poor, dehydrated material and may lack H<sub>2</sub> altogether (Gaidos 2000; Raymond et al. 2007).

The effect of variation in H<sub>2</sub>O abundance on atmospheric escape rates and the evolution of small planets, particularly sub-Neptunes, has not yet been investigated. These effects could be observed around M dwarfs, where the orbital distance corresponding to water condensation falls within the limits of planet detection surveys. Here, we use a model of EUV-driven outflow to demonstrate this effect for temperate sub-Neptunes around M dwarfs, and investigate how it can explain some aspects of exoplanet demographics.

## 2. Model

We used a radially symmetric 1-d model of hydrodynamic escape (Yoshida & Kuramoto 2020; Yoshida et al. 2022), modified for application to sub-Neptunes on close-in orbits around M dwarf stars. Details of the model can be found in Appendix D and these papers. Here we outline the model, focusing on the modifications. We calculated atmospheric escape rates on a coarse, 4-d grid with respect to the stellar EUV flux, planetary gravitational acceleration  $g$ , H<sub>2</sub>O/H<sub>2</sub> ratio at the base of the flow, and planetary mass. Using these rates, we evolved sub-Neptunes with a fixed planetary mass  $M_p$  and on circular orbits around an M2-type (0.45M<sub>⊙</sub>) star, accounting for the (pre-main sequence) evolution in stellar bolometric luminosity, and evolution in stellar EUV luminosity due to rotational spin-down. We adopted  $M_p$  of 2.5 and 5M<sub>⊕</sub>, initial envelope mass fractions of 1–5%, and semi-major axes of 0.01–0.3 au, corresponding to main-sequence stellar irradiance of 0.3–250 times the current terrestrial value. The effect of fixing  $M_p$  on evolutionary calculations was minimal since the atmospheric mass fraction is small. The planetary radius  $R_p$  was calculated as a function of envelope mass fraction, age, and stellar irradiance using the models of Lopez & Fortney (2014). At each time-step, H and O escape rates were calculated by interpolation on the grid, and the envelope mass fraction was adjusted accordingly. For atmospheric evolution calculations, we fixed the basal H<sub>2</sub>O/H<sub>2</sub> ratio, but we investigated the effect of allowing it to increase as a result of H escape in a single, fiducial case.

The atmosphere below the base of the outflow was assumed to be composed only of H<sub>2</sub> and H<sub>2</sub>O. Helium and other carbon- and nitrogen-bearing species are neglected. The lower and upper boundaries of the model are set at radial distances of  $R_p$  and  $50R_p$ , respectively. The number density of H<sub>2</sub> at the lower boundary was set at  $1 \times 10^{13} \text{ cm}^{-3}$ , supposing the typical gas density at the altitude where stellar EUV irradiation is fully absorbed. The H<sub>2</sub>O/H<sub>2</sub> ratio was fixed between 0 and 0.1 in each simulation. This is not equal to the H<sub>2</sub>O/H<sub>2</sub> ratio in the deep atmosphere, i.e., at or below the turbopause where eddy diffusivity mixes atmosphere constituents, but is instead a lower limit (see Discussion). The temperature at the lower boundary was set to the atmospheric skin temperature, which is the asymptotic temperature at high altitudes of the upper atmosphere that is optically thin in the thermal-IR and transparent to shortwave radiation (Catling & Kasting 2017). This basal temperature is 400 K at  $\sim 10\times$  the current terrestrial irradiance. Although this temperature depends on semi-major axis, its variation minimally impacts the outflow structure and escape rate when the escape parameter, the ratio of the planetary gravitational potential energy

to the thermal energy, exceeds  $\sim 10$  (Kubyskhina et al. 2018), as is the case here.

The governing equations in the model are the fluid equations of continuity, momentum, and energy for a multi-component gas, plus those describing chemical reactions and radiative transport, assuming a spherically symmetric geometry. These equations were solved through time-dependent numerical integration until the physical quantities converge to steady profiles, following the calculation method in Yoshida & Kuramoto (2020). The chemical species and reactions considered in this study were the same as in Yoshida et al. (2022). 93 chemical reactions involving 15 species (H<sub>2</sub>, H<sub>2</sub>O, H, O, O(<sup>1</sup>D), OH, O<sub>2</sub>, H<sup>+</sup>, H<sub>2</sub><sup>+</sup>, H<sub>3</sub><sup>+</sup>, O<sup>+</sup>, O<sub>2</sub><sup>+</sup>, OH<sup>+</sup>, H<sub>2</sub>O<sup>+</sup>, and H<sub>3</sub>O<sup>+</sup>, Table D.1 and D.2) are included.

Heating by absorption of stellar X-rays and UV radiation was calculated using a reconstruction of the 0.1–280 nm spectrum of GJ 832 as a representative M2 dwarf (Lloyd et al. 2016). The EUV flux at 1 au is  $1.1 \times 10^{-3} \text{ W m}^{-2}$ , about 25% that of the Sun. For stellar EUV luminosity evolution, we adopt the model of Johnstone et al. (2021) for a star with a mass of 0.4M<sub>⊙</sub> and an initial rotation rate ten times that of the current solar value. To represent both the higher EUV luminosity typical of young stars and a range of semi-major axes, we scaled this spectrum up to  $10^4$  times the current terrestrial irradiance. Heating and photolysis rate profiles were calculated by numerically solving the radiative transfer of parallel stellar photon beams in a spherically symmetric atmosphere, following the method of Tian et al. (2005). The resulting 3-d heating distribution was averaged over spherical shells. Stellar visible and IR radiation was neglected as a heat source in the upper atmosphere. We included radiative cooling by thermal line emission from H<sub>2</sub>O, OH, H<sub>3</sub><sup>+</sup>, OH<sup>+</sup>, and H<sub>3</sub>O<sup>+</sup>, using line data from the HITRAN (Rothman et al. 2013) and ExoMol (Tennyson et al. 2016) databases. In addition to the line emission considered by Yoshida et al. (2022), we included thermal line emission from H<sub>3</sub>O<sup>+</sup> and have expanded the line data for H<sub>2</sub>O and OH to cover a broader temperature range (Appendix D). We calculated radiative cooling rates for these species using the method formulated by Yoshida & Kuramoto (2020).

## 3. Results

### 3.1. Effect of H<sub>2</sub>O abundance on atmospheric escape rates

The escape rate  $\dot{M}$  decreases with increasing basal H<sub>2</sub>O/H<sub>2</sub> ratio due to enhanced radiative cooling and lower temperatures, regardless of gravity or EUV irradiance, with a 1 dex decrease at a basal H<sub>2</sub>O/H<sub>2</sub> ratio of 0.1 relative to a pure H<sub>2</sub> atmosphere (Fig. 1). This reduction in escape rate asymptotes at high H<sub>2</sub>O/H<sub>2</sub> as the outflow becomes optically thick to IR radiation and H<sub>2</sub>O photolysis happens deeper in the outflow due to slower advection. At a given basal H<sub>2</sub>O/H<sub>2</sub> ratio, the escape rate is approximately proportional to  $F_{\text{EUV}}$ , and decreases with increasing  $g$  approximately as  $g^{-3/2}$ , following the expected scaling for energy-limited escape (e.g., Owen 2019). Detailed atmospheric profiles are shown in Appendix A. The escape rate as a function of H<sub>2</sub>O/H<sub>2</sub> ratio,  $F_{\text{EUV}}$ ,  $g$ , and  $M_p$  can be approximated by the following relation:

$$\dot{M} \simeq \dot{M}_{\text{ref}} \left( \frac{F_{\text{EUV}}}{10^3 F_{\text{EUV}}^{\oplus}} \right)^{a_{\text{EUV}}} \left( \frac{g}{4 \text{ m/s}^2} \right)^{-3/2} \left( \frac{M_p}{5M_{\oplus}} \right)^{1/2}, \quad (1)$$

$$\log_{10} \dot{M}_{\text{ref}} [\text{M}_{\oplus}/\text{Gyr}] = 0.01042(\log_{10} r)^3 + 0.1257(\log_{10} r)^2 + 0.2429 \log_{10} r - 1.311, \quad (2)$$

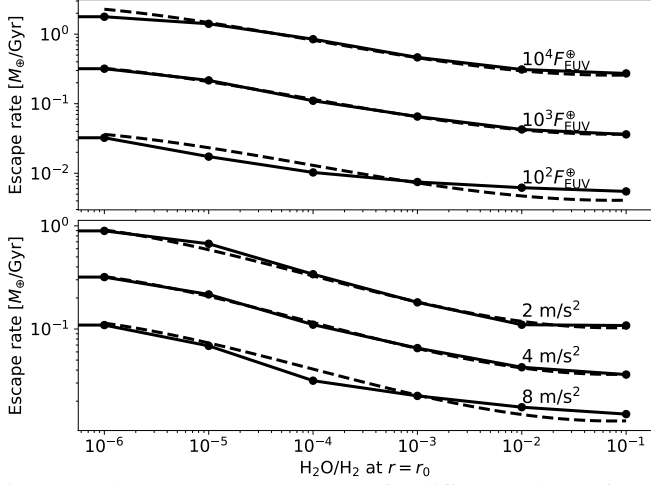


Fig. 1: Total escape rate vs.  $\text{H}_2\text{O}/\text{H}_2$  for different values of EUV irradiance at fixed surface gravity  $g = 4 \text{ m s}^{-2}$  (top panel) and for different values of  $g$  at a fixed EUV irradiance of  $10^3 F_{\oplus}$  (bottom panel).  $M_p$  is fixed at  $5M_{\oplus}$ . The dashed lines are from Eqns. 1–3.

$$a_{\text{EUV}} = -0.05 \log_{10} \left( \frac{F_{\text{EUV}}}{10^3 F_{\oplus}^{\text{EUV}}} \right) + 0.9, \quad (3)$$

where  $F_{\text{EUV}}^{\oplus}$  is the EUV flux at Earth and  $r$  is the basal  $\text{H}_2\text{O}/\text{H}_2$  ratio.  $a_{\text{EUV}}$  decreases with increasing  $F_{\text{EUV}}$  because as temperature increases, radiative cooling becomes more effective (Yoshida & Kuramoto 2021). This function may become invalid under thermally unstable conditions (Kubyskhina et al. 2018), extremely high EUV flux and deep gravitational potential conditions such as those of hot Jupiters where atomic cooling is effective (Murray-Clay et al. 2009; Salz et al. 2016), and in the diffusion-limited regime (Hunten 1973).

### 3.2. $\text{H}_2\text{O}/\text{H}_2$ -dependent evolution of sub-Neptunes

Figure 2 shows the evolutionary tracks of atmospheres with different  $\text{H}_2\text{O}/\text{H}_2$  ratios for  $M_p = 2.5M_{\oplus}$  and a 1% initial envelope mass fraction, on an orbit where the main sequence stellar flux is equivalent to the solar constant. High  $\text{H}_2\text{O}/\text{H}_2$  ratios extend atmospheric lifetimes by reducing escape rates through radiative cooling (Fig. 2b). For  $\text{H}_2\text{O}/\text{H}_2$  ratios above  $10^{-3}$ , envelopes persist for at least 10 Gyr, whereas atmospheres with lower  $\text{H}_2\text{O}/\text{H}_2$  ratios are lost within the period (Fig. 2c). If mass fractionation between H and O is included (Appendix B), atmospheric lifetimes slightly increase as the  $\text{H}_2\text{O}/\text{H}_2$  ratio increases (dashed lines in Fig. 2c). Planets that retain significant envelopes have radii  $\geq 2R_{\oplus}$  (Fig. 2d).

Figure 3 shows envelope lifetime as a function of stellar irradiance and the  $\text{H}_2\text{O}/\text{H}_2$  ratio, where the lifetime is defined as the time when the atmospheric mass falls below  $10^{-4} M_p$ . The three scenarios in Fig. 2 with  $\text{H}_2\text{O}/\text{H}_2 > 0$  are plotted as stars. The timescale increases with  $\text{H}_2\text{O}/\text{H}_2$  and decreases with irradiance. The lifetime is weakly dependent on the initial envelope mass due to the dependence of gravity on planet radius and hence on envelope mass (Fig. C.1).

## 4. Discussion

Around low luminosity K- and M dwarfs, temperate planets in which  $\text{H}_2\text{O}$  condensation will limit the abundance in their upper atmospheres at  $\lesssim 0.3 \text{ au}$ , within the range probed by exoplanet

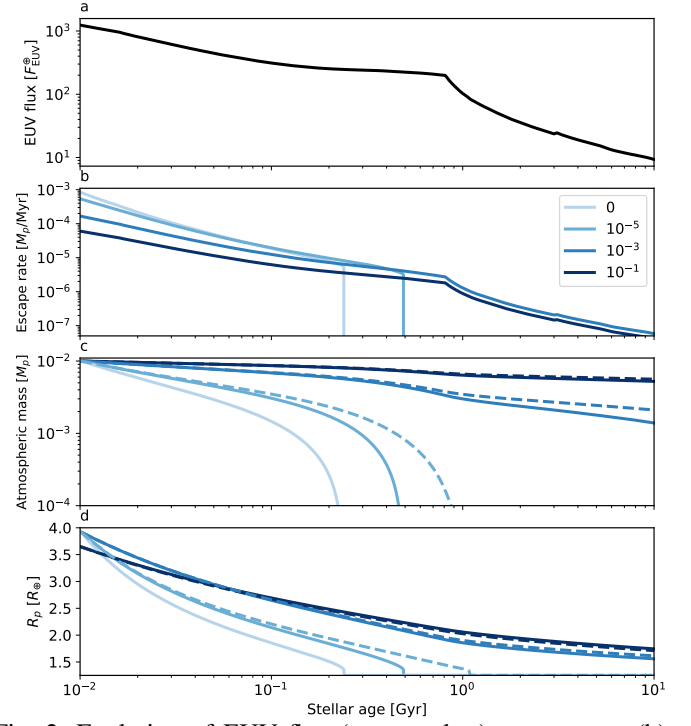


Fig. 2: Evolution of EUV flux (top panel, a), escape rate (b), envelope mass (c), and planet radius (d) for a planet with  $M_p = 2.5M_{\oplus}$ , an initial envelope mass fraction of 1%, and different initial values of  $\text{H}_2\text{O}/\text{H}_2$  on an orbit with a main-sequence stellar irradiance equal to the terrestrial value. Solid (dashed) lines represent results without (with) mass fractionation between H and O. The mass fractionation results have been omitted from panel b for clarity.

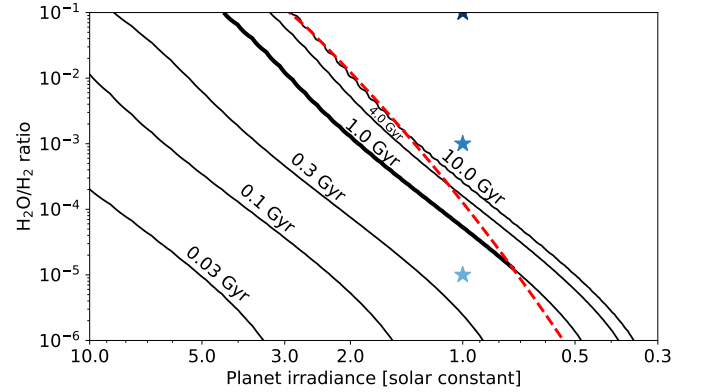


Fig. 3: Lifetime of envelopes with initial mass fraction of 1% on  $M_p = 2.5M_{\oplus}$  sub-Neptunes as a function of stellar irradiance and  $\text{H}_2\text{O}/\text{H}_2$ . The dashed line is the saturation-limited  $\text{H}_2\text{O}/\text{H}_2$  ratio in the upper atmosphere (see text and Appendix C). The stars represent the scenarios in Fig. 2.

surveys such as *Kepler*. Gaidos et al. (2024) showed that the radius distribution of close-in planets around single M dwarfs, like that of solar-type stars, includes two peaks representing super-Earths and sub-Neptunes (see also Hirano et al. 2018; Cloutier & Menou 2020; Van Eylen et al. 2021). Using stellar-rotation based ages, Gaidos et al. (2023) found that the younger half of the sample (mean age of  $\sim 2.5$  Gyr) contains more sub-Neptunes relative to super-Earths than the older half (mean age of  $\sim 6$  Gyr). This trend is similar to that found around solar-type stars (e.g., Berger et al. 2020), and expected from models

in which sub-Neptunes lose their envelopes to EUV-driven escape and evolve into super-Earths. Unexpectedly, Gaidos et al. (2024) found that the disappearance of sub-Neptunes occurs primarily at larger distances and lower irradiance, near the point where  $\text{H}_2\text{O}$  is expected to condense in the atmospheres of temperate planets. They speculated that the disappearance of cooler sub-Neptunes over Gyr timescales could be due to the collapse of steam-dominated atmospheres, or the accelerated loss of  $\text{H}$ -rich atmospheres from which  $\text{H}_2\text{O}$  has condensed.

As shown in Fig. 3, envelopes are rapidly ( $\ll 1$  Gyr) lost from planets that are highly irradiated ( $S > 5S_\oplus$ ) and/or are  $\text{H}_2\text{O}$ -poor. The dashed curve is the upper atmosphere saturation-limited  $\text{H}_2\text{O}$  concentration as a function of irradiance (i.e., planet equilibrium temperature) predicted by a simple model of a  $\text{H}_2$ -dominated radiative-convective atmosphere with a Bond albedo equal to that of Neptune (see Appendix E for details). The location of the curve with respect to the contours of envelope lifetime suggests that a sub-Neptune irradiated at greater than the solar constant would retain its envelope and large radius for  $\geq 4$  Gyr due to cooling by  $\text{H}_2\text{O}$ . The same object at greater distances and lower irradiance would lose its envelope in  $< 4$  Gyr, possibly explaining the paradoxical findings of Gaidos et al. (2024).<sup>2</sup> Cooling by other, less condensible molecules (e.g.,  $\text{CO}$ ,  $\text{CH}_4$ ) will be important at low  $\text{H}_2\text{O}/\text{H}_2$  (see below), such that the contours in Fig. 3 should become vertical, i.e., envelopes can persist at yet further distances.

Fig. 4a demonstrates that, even if envelopes survive, the saturation-limited abundance of  $\text{H}_2\text{O}$  affects the radii and hence detectability by transit of sub-Neptunes observed at ages typical of *Kepler* target stars (e.g., Dressing & Charbonneau 2015; Ment & Charbonneau 2023). It shows the radius of  $2.5M_\oplus$  sub-Neptunes vs. irradiance, for envelope mass fractions of 1% and 3% and  $\text{H}_2\text{O}/\text{H}_2$  set by the saturation limit, after 2 Gyr and 6 Gyr of evolution. At a given age, radii increase with decreasing (EUV) irradiance (due to increasing distance) until reaching an age- and envelope mass fraction-dependent maximum at twice the solar constant. Thereafter the radius declines as decreasing (bolometric) irradiance and equilibrium temperatures suppress  $\text{H}_2\text{O}$  and its cooling of the upper atmosphere. Below an irradiance of  $\sim 50\%$  the solar constant, cooling by  $\text{H}_2\text{O}$  is negligible and radii again increase with declining EUV flux.

In water-poor systems, inefficient cooling will render primordial  $\text{H}/\text{He}$  envelopes around rocky cores more susceptible to hydrodynamic escape (Fig. 4b) as well as erosion by stellar winds. Infrared spectroscopy by *Spitzer* and *JWST* has revealed that the chemistry of many inner protoplanetary disks around very low mass stars (VLMS,  $\leq 0.2M_\odot$ ) is consistent with a high C/O ratio (Najita et al. 2013; Tabone et al. 2023; Arabhavi et al. 2024; Kanwar et al. 2024; Long et al. 2025). Sub-Neptunes arising from such disks could have high C/O,  $\text{H}_2\text{O}$ -poor envelopes. Figure 4b shows that, on orbits with super-terrestrial irradiance ( $< 0.06$  au for an  $M_2$ -type host) where planets are readily detected by transit surveys, such envelopes will completely escape by 4 Gyr. While temperate, C/O-rich sub-Neptunes are predicted to contain abundant  $\text{CH}_4$  (Moses et al. 2013), this molecule is a less efficient radiator and susceptible to UV photodissociation (Yoshida et al. 2024b,a).  $\text{CO}$  from disequilibrium mixing (Fortney et al. 2020) could be a source of  $\text{O}$  for the formation of  $\text{H}_2$  and  $\text{OH}$ , but its high molecular weight will limit its altitude

<sup>2</sup> At  $\text{H}_2\text{O}/\text{H}_2$  exceeding 0.1 the metallicity is  $> 100$ , the molecular weight is more than doubled, and due to that and increased cooling planets are less likely to have extended sub-Neptune-like atmospheres (Linssen et al. 2024).

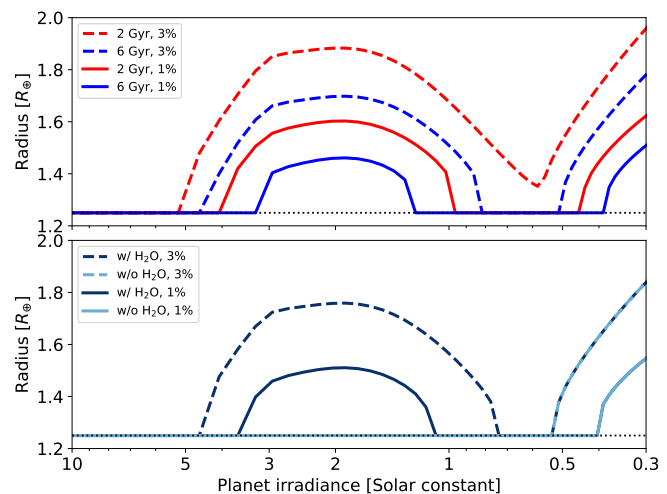


Fig. 4: Top (a): Planet radius vs. irradiance for sub-Neptunes with a mass of  $2.5M_\oplus$  and initial envelope mass fractions of 1% (solid lines) and 3% (dashed lines), at 2 and 6 Gyr.  $\text{H}_2\text{O}/\text{H}_2$  is set to the saturation limit (dashed line in Fig. 3) up to a maximum of 0.1. Bottom (b): Same for sub-Neptunes at 4 Gyr with  $\text{H}_2\text{O}$  as prescribed above, vs. those having envelopes without  $\text{H}_2\text{O}$ .

distribution to the turbopause, where  $\text{CO}$ -dissociating far-UV photons are already absorbed by overlying  $\text{CH}_4$ . Thus planets forming from high C/O disks will experience accelerated evaporation of their envelopes, which might explain the paucity of sub-Neptunes relative to rocky planets around VLMS compared to their FGK counterparts (Ment & Charbonneau 2023). Not all disks around VLMS are O-poor (Xie et al. 2023) and such exceptions could give rise to a surviving population of  $\text{H}_2\text{O}$ -rich (or at least metal-rich) sub-Neptunes, e.g. GJ 1214b (Ohno et al. 2025).

In the same vein, protoplanetary disks around stars in binary systems with separations much less than  $\sim 100$  au are tidally truncated to a few au and are shorter lived (see Zagaria et al. 2023, and references therein). In these cases, the removal of icy, O-rich ( $\text{H}_2\text{O}$  and  $\text{CO}_2$ ) solids in the outer disk that would otherwise drift inward could lead to O- and  $\text{H}_2\text{O}$ -poor planets in the inner disk. These  $\text{H}_2\text{O}$ -poor objects would experience more rapid envelope escape, possibly explaining the deficit of detectable planets in such systems (Kraus et al. 2016), and in particular lack of sub-Neptunes relative to super-Earths (Sullivan et al. 2023).

The predicted decline in the abundance of  $\text{H}_2\text{O}$  at irradiances below  $\sim 3$  times the solar constant (Fig. 3) can be detected by *JWST* using the method of transmission spectroscopy during transits (e.g. Benneke et al. 2024; Holmberg & Madhusudhan 2024); such observations probe atmospheric composition at the 1–10 mbar level (Beichman & Greene 2018). All else being equal, indicators of atmospheric escape, e.g., anomalous absorption in  $\text{H}$  Lyman- $\alpha$  or the  $\text{He}$  triplet at 1083 nm should be anti-correlated with the presence of  $\text{H}_2\text{O}$ .

One caveat of our work is that we show outcomes for specific envelope mass fractions, whereas a population of sub-Neptunes would presumably have a distribution of values. Nevertheless, the overall trends with  $\text{H}_2\text{O}/\text{H}_2$ , irradiation, and stellar mass should hold. Another is that the saturation concentration of  $\text{H}_2\text{O}$  at the radiative-convective boundary should be considered an upper limit to the value in the upper atmosphere. The lower simulation boundary where  $\text{H}_2\text{O}/\text{H}_2$  is fixed is at a number density of  $\sim 10^{13} \text{ cm}^{-3}$  and an altitude above the turbopause where the atmosphere ceases to be well mixed. Based on the eddy diffu-

sivity relation for solar-metallicity atmospheres in Charnay et al. (2015) and a molecular diffusivity for H<sub>2</sub> (Suárez-Iglesias et al. 2015), the turbopause is predicted to lie at a pressure altitude of  $8.7 \times 10^{-5}$  bar or a density of  $2.3 \times 10^{15}$  cm<sup>-3</sup>. This corresponds to several scale heights below the base of the thermosphere, and could mean that H<sub>2</sub>O is significantly depleted by diffusion. H<sub>2</sub>O is also photo-dissociated by FUV radiation, but in a H-rich atmosphere the back reaction is efficient, and there should be an equilibrium between H<sub>2</sub>O and the principle photodissociation product O<sub>2</sub> (e.g., Kawamura et al. 2024). An O<sub>2</sub>-rich layer will form on top of the H<sub>2</sub>O-rich atmosphere below and protect it from FUV radiation (inset of top panel of Fig. A.2). Finally, above a critical H<sub>2</sub>O/H<sub>2</sub>( $10^{-2}$  for solar metallicity and higher for super-solar), moist convection will be inhibited (Guillot 1995; Leconte et al. 2017), altering the pressure-temperature profile.

## 5. Conclusions

The hydrodynamic escape of H and He thought to be responsible for the evolution of gas-rich sub-Neptunes into rocky-dominated super-Earths is governed by the stellar EUV energy absorbed in the upper atmosphere relative to the energy of escape from planetary gravity. This balance is modulated by IR and line emission by molecules and ions within the flow. We use a hydrodynamic escape model of a spherically symmetric, EUV-driven wind to demonstrate that the abundance of H<sub>2</sub>O in the upper atmosphere has a significant effect on escape rates. Specifically, we find that:

- An increase in the H<sub>2</sub>O abundance from  $10^{-6}$  to  $10^{-1}$  leads to a one dex decrease in escape rate, irrespective of surface gravity and XUV flux.
- Sub-Neptunes just outside an irradiance level, approximately the solar constant, where saturation severely limits the H<sub>2</sub>O concentration in the upper atmosphere will experience rapid decline in their radii relative to equivalent planets slightly closer to their host stars, potentially explaining the evolutionary trends inferred by Gaidos et al. (2024).
- Sub-Neptunes that form around very low mass stars ( $\lesssim 0.2M_{\odot}$ ), which tend to have protoplanetary disks with H<sub>2</sub>O-poor chemistries consistent with a high C/O ratio, are likely to experience more rapid escape, a possible explanation for their paucity around such stars.
- A spectroscopic investigation of temperate sub-Neptune envelopes, i.e. by *JWST*, should reveal a marked decline in water content with lower irradiance, correlating with the paucity of such objects around older stars.

*Acknowledgements.* TY was supported by JSPS KAKENHI Grant Nos. 23KJ0093 and 23H04645. EG was supported by NASA Awards 80NSSC20K0957 (Exoplanets Research Program) and 80NSSC21K0597 (Interdisciplinary Consortia for Astrobiology Research) and as a Gauss Professor at the University of Göttingen by the Niedersächsische Akademie der Wissenschaften.

## References

Arabhavi, A. M., Kamp, I., Henning, T., et al. 2024, *Science*, 384, 1086  
 Banks, P. M. & Kockarts, G. 1973, *Aeronomy* (Elsevier)  
 Beichman, C. A. & Greene, T. P. 2018, in *Handbook of Exoplanets*, ed. H. J. Deeg & J. A. Belmonte, 85  
 Benneke, B., Roy, P.-A., Coulombe, L.-P., et al. 2024, arXiv e-prints, arXiv:2403.03325  
 Berger, T. A., Huber, D., van Saders, J. L., et al. 2020, *AJ*, 159, 280  
 Bohren, C. F. & Albrecht, B. A. 1998, *Atmospheric thermodynamics*  
 Catling, D. C. & Kasting, J. F. 2017, *Atmospheric evolution on inhabited and lifeless worlds* (Cambridge University Press)

Charnay, B., Meadows, V., & Leconte, J. 2015, *ApJ*, 813, 15  
 Cloutier, R. & Menou, K. 2020, *AJ*, 159, 211  
 Dressing, C. D. & Charbonneau, D. 2015, *ApJ*, 807, 45  
 Fortney, J. J., Visscher, C., Marley, M. S., et al. 2020, *AJ*, 160, 288  
 Fulton, B. J., Petigura, E. A., Howard, A. W., et al. 2017, *AJ*, 154, 109  
 Gaidos, E., Ali, A., Kraus, A. L., & Rowe, J. F. 2024, *MNRAS*, 534, 3277  
 Gaidos, E., Claytor, Z., Dungee, R., Ali, A., & Feiden, G. A. 2023, *MNRAS*, 520, 5283  
 Gaidos, E., Hirano, T., Beichman, C., et al. 2022, *MNRAS*, 509, 2969  
 Gaidos, E. J. 2000, *Icarus*, 145, 637  
 Guillot, T. 1995, *Science*, 269, 1697  
 Hirano, T., Dai, F., Gandolfi, D., et al. 2018, *AJ*, 155, 127  
 Hirano, T., Livingston, J. H., Fukui, A., et al. 2021, *AJ*, 162, 161  
 Holmberg, M. & Madhusudhan, N. 2024, *A&A*, 683, L2  
 Howard, A. W., Marcy, G. W., Bryson, S. T., et al. 2012, *ApJS*, 201, 15  
 Huebner, W. & Mukherjee, J. 2015, *Planetary and Space Science*, 106, 11  
 Hunte, D. M. 1973, *Journal of Atmospheric Sciences*, 30, 1481  
 Johnstone, C. P., Bartel, M., & Güdel, M. 2021, *A&A*, 649, A96  
 Johnstone, C. P., Güdel, M., Lammer, H., & Kislyakova, K. G. 2018, *A&A*, 617, A107  
 Kanwar, J., Kamp, I., Jang, H., et al. 2024, *A&A*, 689, A231  
 Kasting, J. F. 1988, *Icarus*, 74, 472  
 Kawamura, Y., Yoshida, T., Terada, N., et al. 2024, *The Astrophysical Journal*, 967, 95  
 Kockarts, G. 1980, *Geophys. Res. Lett.*, 7, 137  
 Kraus, A. L., Ireland, M. J., Huber, D., Mann, A. W., & Dupuy, T. J. 2016, *AJ*, 152, 8  
 Kubyschkina, D., Fossati, L., Erkaev, N. V., et al. 2018, *Astronomy & Astrophysics*, 619, A151  
 Kuramoto, K., Umemoto, T., & Ishiwatari, M. 2013, *Earth and Planetary Science Letters*, 375, 312  
 Le Teuff, Y., Millar, T., & Markwick, A. 2000, *Astronomy and Astrophysics Supplement Series*, 146, 157  
 Leconte, J., Selsis, F., Hersant, F., & Guillot, T. 2017, *A&A*, 598, A98  
 Linssen, D., Shih, J., MacLeod, M., & Oklopčić, A. 2024, *A&A*, 688, A43  
 Long, F., Pascucci, I., Houge, A., et al. 2025, *ApJ*, 978, L30  
 Lopez, E. D. & Fortney, J. J. 2014, *The Astrophysical Journal*, 792, 1  
 Loyd, R. P., France, K., Youngblood, A., et al. 2016, *The Astrophysical Journal*, 824, 102  
 Masson, A., Vinatier, S., Bézard, B., et al. 2024, *A&A*, 688, A179  
 McElroy, D., Walsh, C., Markwick, A., et al. 2013, *Astronomy & Astrophysics*, 550, A36  
 Ment, K. & Charbonneau, D. 2023, *AJ*, 165, 265  
 Mlynczak, M. G., Hunt, L. A., Garcia, R. R., et al. 2022, *Journal of Geophysical Research (Atmospheres)*, 127, e2022JD036767  
 Moses, J. I., Line, M. R., Visscher, C., et al. 2013, *ApJ*, 777, 34  
 Muñoz, A. G. 2007, *Planetary and Space Science*, 55, 1426  
 Murray-Clay, R. A., Chiang, E. I., & Murray, N. 2009, *ApJ*, 693, 23  
 Najita, J. R., Carr, J. S., Pontoppidan, K. M., et al. 2013, *ApJ*, 766, 134  
 Ohno, K., Schlawin, E., Bell, T. J., et al. 2025, *ApJ*, 979, L7  
 Orell-Miquel, J., Lampón, M., López-Puertas, M., et al. 2023, *A&A*, 677, A56  
 Owen, J., Shaikhislamov, I., Lammer, H., Fossati, L., & Khodachenko, M. 2020, *Space Science Reviews*, 216, 1  
 Owen, J. E. 2019, *Annual Review of Earth and Planetary Sciences*, 47, 67  
 Owen, J. E. & Wu, Y. 2013, *ApJ*, 775, 105  
 Petigura, E. A., Howard, A. W., & Marcy, G. W. 2013, *Proceedings of the National Academy of Science*, 110, 19273  
 Petigura, E. A., Rogers, J. G., Isaacson, H., et al. 2022, *AJ*, 163, 179  
 Piaulet-Ghorayeb, C., Benneke, B., Radica, M., et al. 2024, *ApJ*, 974, L10  
 Pierrehumbert, R. T. 2023, *ApJ*, 944, 20  
 Raymond, S. N., Scalo, J., & Meadows, V. S. 2007, *ApJ*, 669, 606  
 Robinson, T. D. & Catling, D. C. 2012, *ApJ*, 757, 104  
 Roble, R. G. & Dickinson, R. E. 1989, *Geophys. Res. Lett.*, 16, 1441  
 Rockcliffe, K. E., Newton, E. R., Youngblood, A., et al. 2023, *AJ*, 166, 77  
 Rothman, L. S., Gordon, I. E., Babikov, Y., et al. 2013, *J. Quant. Spectr. Rad. Transf.*, 130, 4  
 Salz, M., Schneider, P., Czesla, S., & Schmitt, J. 2016, *Astronomy & Astrophysics*, 585, L2  
 Suárez-Iglesias, O., Medina, I., Sanz, M. d. I. A., Pizarro, C., & Bueno, J. L. 2015, *Journal of Chemical & Engineering Data*, 60, 2757  
 Sullivan, K., Kraus, A. L., Huber, D., et al. 2023, *AJ*, 165, 177  
 Tabone, B., Bettoni, G., van Dishoeck, E. F., et al. 2023, *Nature Astronomy*, 7, 805  
 Tennyson, J., Yurchenko, S. N., Al-Refaie, A. F., et al. 2016, *Journal of Molecular Spectroscopy*, 327, 73  
 Tian, F., Toon, O. B., Pavlov, A. A., & De Sterck, H. 2005, *The Astrophysical Journal*, 621, 1049  
 Turbet, M., Bolmont, E., Ehrenreich, D., et al. 2020, *A&A*, 638, A41  
 Van Eylen, V., Astudillo-Defru, N., Bonfils, X., et al. 2021, *MNRAS*, 507, 2154  
 Venturini, J., Ronco, M. P., Guilera, O. M., et al. 2024, *A&A*, 686, L9

- Weiss, L. M. & Marcy, G. W. 2014, *ApJ*, 783, L6
- Xie, C., Pascucci, I., Long, F., et al. 2023, *ApJ*, 959, L25
- Yabe, T. & Aoki, T. 1991, *Computer physics communications*, 66, 219
- Yoshida, T., Koyama, S., Nakamura, Y., Terada, N., & Kuramoto, K. 2024a, *Astrobiology*, 24, 1074
- Yoshida, T. & Kuramoto, K. 2020, *Icarus*, 345, 113740
- Yoshida, T. & Kuramoto, K. 2021, *Monthly Notices of the Royal Astronomical Society*, 505, 2941
- Yoshida, T., Terada, N., Ikoma, M., & Kuramoto, K. 2022, *ApJ*, 934, 137
- Yoshida, T., Terada, N., & Kuramoto, K. 2024b, *Progress in Earth and Planetary Science*, 11, 59
- Zagaria, F., Rosotti, G. P., Alexander, R. D., & Clarke, C. J. 2023, *European Physical Journal Plus*, 138, 25
- Zhang, M., Knutson, H. A., Dai, F., et al. 2023, *AJ*, 165, 62

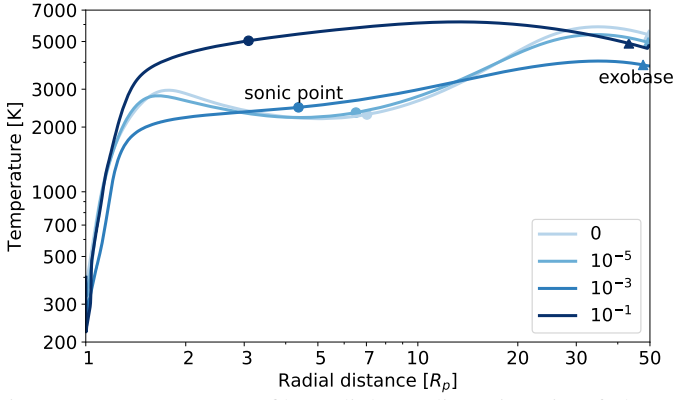


Fig. A.1: Temperature profile (radial coordinate in units of planet radius) in a hydrodynamic flow for different lower boundary values  $\text{H}_2\text{O}/\text{H}_2$  with a stellar EUV flux of  $1000F_{\text{EUV}}^{\oplus}$ ,  $M_p = 5M_{\oplus}$ , and  $g = 4 \text{ m s}^{-2}$ , where  $F_{\text{EUV}}^{\oplus}$  is the present EUV flux at Earth. Sonic points are marked by filled circles and the exobase is marked by triangles.

## Appendix A: Atmospheric Profiles

Fig. A.1 shows the dependence of the outflow temperature profile on basal  $\text{H}_2\text{O}/\text{H}_2$  subjected to stellar EUV  $10^3\times$  the present terrestrial value, with  $M_p = 5M_{\oplus}$  and  $g = 4 \text{ m s}^{-2}$ . Fig. A.2 shows profiles of the number density, heating, and cooling rate in a flow with the same parameters, except only for a basal  $\text{H}_2\text{O}/\text{H}_2$  ratio of  $10^{-3}$ . In the lower region of the flow ( $r \lesssim 2R_p$ ), the temperature decreases with increasing basal  $\text{H}_2\text{O}/\text{H}_2$  ratio up to  $\sim 0.01$  as a result of greater radiative cooling. As shown in Fig. A.2,  $\text{H}_2\text{O}$  is the primary coolant in this lower region. Along the outflow,  $\text{H}_2\text{O}$  is photolyzed to H, O, OH, and various ions. As a result, cooling by photochemical products, especially  $\text{H}_3^+$  and  $\text{OH}^+$ , is significant at higher altitudes. As the basal  $\text{H}_2\text{O}/\text{H}_2$  ratio approaches  $\sim 0.1$ , the mean molecular weight of the flow increases, reducing the speed of the outflow and the contribution of adiabatic cooling, and temperatures in the lower region of the flow begin to increase. This dependence on the mean molecular weight is discussed in detail by Yoshida & Kuramoto (2020).

## Appendix B: Mass fractionation between H and O

Fig. B.1 shows the fractionation factor between H and O, defined as  $(F_{\text{O}}/F_{\text{H}})/(n_{\text{O}}(r_0)/n_{\text{H}}(r_0))$ , where  $F_i$  and  $n_i(r_0)$  are the escape rate and the total number density at the lower boundary  $r_0$  of element  $i$ , respectively. This ratio decreases (fractionation increases) as the  $\text{H}_2\text{O}/\text{H}_2$  ratio increases or as the EUV flux decreases, due to the reduced H escape flux and less efficient O drag.

## Appendix C: Escape timescale as a function of initial atmospheric mass and stellar flux

Fig. C.1 shows the escape timescale of pure  $\text{H}_2$  atmosphere as a function of stellar flux and initial atmospheric mass with a planetary mass of  $2.5M_p$ , where the timescale is defined as the duration required for the atmospheric mass to reach  $10^{-4}M_p$ . The timescale exhibits weak dependence on the initial atmospheric mass because the escape rate increases with initial atmospheric mass due to planetary inflation and the resulting decrease in gravitational acceleration at the base of the outflow.

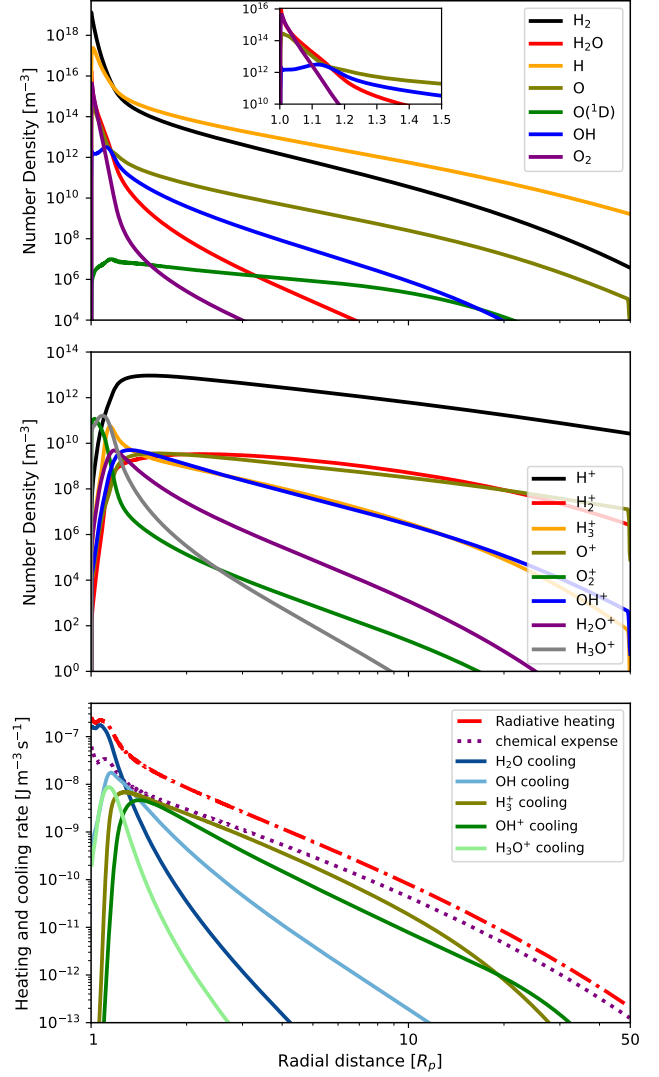


Fig. A.2: Top: Number density profiles of neutral species with a basal  $\text{H}_2\text{O}/\text{H}_2$  of 0.001, stellar EUV flux of  $1000F_{\text{EUV}}^{\oplus}$ ,  $M_p = 5M_{\oplus}$ , and  $g = 4 \text{ m s}^{-2}$ . The inset panel shows details near the base of the flow. Middle: Predicted number density profiles of ions. Bottom: Contribution of these species to cooling rates. “Radiative heating” is the heating rate by adsorption of X-rays and UV, and “chemical expense” is the energy used by chemical reactions such as photolysis.

## Appendix D: Model details

### D.1. Basic equations

We solve the fluid equations of continuity, momentum and energy for a multi-component gas, assuming a spherically symmetric flow:

$$\frac{\partial n_i}{\partial t} + \frac{1}{r^2} \frac{\partial (n_i u_i r^2)}{\partial r} = \omega_i, \quad (\text{D.1})$$

$$\frac{\partial u_i}{\partial t} + u_i \frac{\partial u_i}{\partial r} = -\frac{1}{\rho_i} \frac{\partial p_i}{\partial r} - \frac{GM_p}{r^2} + \sum_j (u_j - u_i) \frac{n_j}{m_i} \mu_{ij} k_{ij}, \quad (\text{D.2})$$

$$\frac{\partial}{\partial t} \left[ \rho \left( \frac{1}{2} u^2 + E \right) \right] + \frac{1}{r^2} \frac{\partial}{\partial r} \left\{ \left[ \left( \frac{1}{2} u^2 + E + \frac{p}{\rho} \right) \rho u \right] r^2 \right\} = -\frac{GM_p}{r^2} \rho u + q,$$

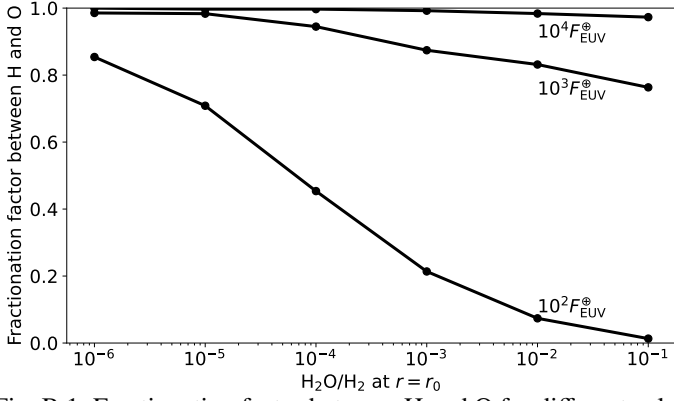


Fig. B.1: Fractionation factor between H and O for different values of interior  $\text{H}_2\text{O}/\text{H}_2$  and stellar EUV flux with a surface gravity of  $4 \text{ m s}^{-2}$  and planet mass of  $5M_{\oplus}$ .

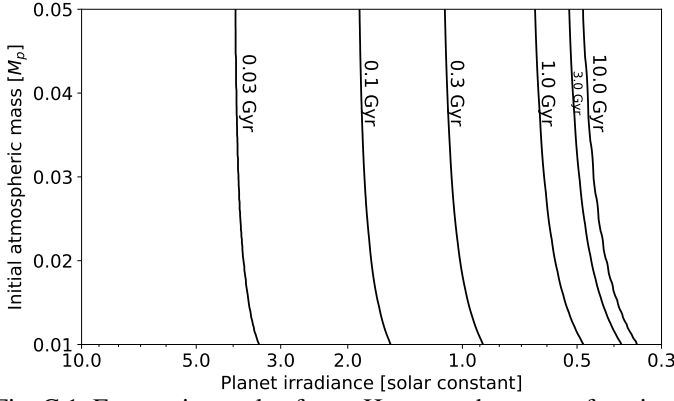


Fig. C.1: Escape timescale of pure  $\text{H}_2$  atmospheres as a function of stellar irradiance and initial envelope mass with a planet mass of  $2.5M_{\oplus}$ .

$$(D.3)$$

where  $t$  is the time,  $r$  is the distance from the planet's center,  $n_i$ ,  $\rho_i$ ,  $u_i$ ,  $p_i$ , and  $\omega_i$  are the number density, mass density, velocity, partial pressure, and production rate of species  $i$ , respectively,  $G$  is the gravitational constant,  $M_p$  is the mass of the planet,  $\rho$ ,  $p$ , and  $E$  are the total mass density, total pressure, and total specific internal energy, respectively,  $u$  is the mean gas velocity,  $\mu_{ij}$  is the reduced molecular mass between species  $i$  and  $j$ ,  $k_{ij}$  is the momentum transfer collision frequency that follows

$$k_{ij} = \frac{k_B T}{\mu_{ij} b_{ij}}, \quad (D.4)$$

where  $k_B$  is the Boltzmann constant and  $T$  is the temperature.  $b_{ij}$  is the binary diffusion coefficient given by

$$b_{ij} = \begin{cases} 1.96 \times 10^6 \frac{T^{1/2}}{\mu_{ij}} & \text{for neutral-neutral pair} \\ 4.13 \times 10^{-8} \frac{T}{\mu_{ij}^{1/2} \alpha^{1/2}} & \text{for neutral-ion pair} \\ 8.37 \times 10^{-5} \frac{T^{3/2}}{\mu_{ij}} & \text{for ion-ion pair} \end{cases} \quad (D.5)$$

where  $\alpha$  is the polarizability (Banks & Kockarts 1973; Muñoz 2007). Here,  $b_{ij}$ ,  $T$ ,  $\mu_{ij}$  and  $\alpha$  are expressed in  $\text{cm}^{-1}\text{s}^{-1}$ , K, g and  $\text{cm}^3$ , respectively. The total internal energy is given by

$$\rho E = \frac{1}{n} \left( \sum_i \frac{n_i}{\gamma_i - 1} \right) p, \quad (D.6)$$

where  $n$  is the total number density and  $\gamma_i$  is the ratio of specific heat of species  $i$ . The net heating rate is given by

$$q = q_{\text{abs}} - q_{\text{ch}} - q_{\text{rad}}, \quad (D.7)$$

where  $q_{\text{abs}}$  is the heating rate by X-ray and UV absorption (see D.3),  $q_{\text{ch}}$  is the rate of net chemical expense of energy (see D.2), and  $q_{\text{rad}}$  is the radiative cooling rate by IR active molecules (see D.3).

## D.2. Chemistry

A total of 93 chemical reactions are considered for 15 atmospheric components:  $\text{H}_2$ ,  $\text{H}_2\text{O}$ , H, O,  $\text{O}(^1\text{D})$ , OH,  $\text{O}_2$ ,  $\text{H}^+$ ,  $\text{H}_2^+$ ,  $\text{H}_3^+$ ,  $\text{O}^+$ ,  $\text{O}_2^+$ ,  $\text{OH}^+$ ,  $\text{H}_2\text{O}^+$ , and  $\text{H}_3\text{O}^+$  (Table A1 and A2).

The photolysis rate  $f_{\text{ph},i}$  is given by

$$f_{\text{ph},i} = \int_{\lambda} n_i \sigma_i(\lambda) I(\lambda) d\lambda, \quad (D.8)$$

where  $\sigma_i(\lambda)$  is the photodissociation/photoionization cross section at wavelength  $\lambda$  for species  $i$  and  $I(\lambda)$  is the incident X-ray/UV photon flux at wavelength  $\lambda$ . The energy consumed per unit time by this photolysis  $q_{\text{ph},i}$  is given by

$$q_{\text{ph},i} = f_{\text{ph},i} \frac{hc}{\lambda_{\text{th},i}}, \quad (D.9)$$

where  $\lambda_{\text{th},i}$  is the threshold wavelength for the photolysis of species  $i$ ,  $h$  is the Planck constant, and  $c$  is the speed of light in vacuum. We adopt the photodissociation and photoionization cross sections provided by ‘‘PHoto Ionization/Dissociation RATES’’ (Huebner & Mukherjee 2015; <http://phidrates.space.swri.edu>).

In addition to photolysis reactions, this study considers bimolecular reactions. The bimolecular reaction rate  $f_R$  can be written as

$$f_R = k_R n_i n_j, \quad (D.10)$$

where  $n_i$  and  $n_j$  represent the number densities of reactant  $i$  and  $j$ , respectively, and  $k_R$  is the corresponding reaction rate coefficient. We use the reaction rate coefficients provided by ‘‘The UMIST Database for Astrochemistry 2012’’ (McElroy et al. 2013; <http://udfa.a.jmarkwick.net>). We neglect the formation of molecules that have more than one carbon atom because of the low densities in the outflow. The energy consumed per unit time by a bimolecular reaction is given by

$$q_R = -f_R \Delta E_R, \quad (D.11)$$

where  $\Delta E_R$  is the heat of reaction, which is positive for endothermic reactions and negative for exothermic reactions. In evaluating the heats of reaction, we make use of the enthalpies of formation listed in Le Teuff et al. (2000). The energy consumption rate  $q_{\text{ch}}$  is calculated by summing the consumed amounts of energy by individual chemical reactions including photolysis.

## D.3. Radiative processes

In order to calculate the radial profiles of rates of heating and photolysis in the atmosphere, we model the radiative transfer of parallel stellar photon beams in a spherically symmetric atmosphere by applying the method formulated by Tian et al. (2005). We consider X-ray and UV absorption by  $\text{H}_2$ ,  $\text{H}_2\text{O}$ , H, O, OH, and  $\text{O}_2$ . The stellar beam is assumed to be absorbed by Beer's

law. The energy deposition in a given layer along each path is then multiplied by the area of the ring (Fig. 6 in Tian et al. 2005) to obtain the total energy deposited into the shell segment. The volumetric heating rate  $q_{\text{abs}}$  is given by the total energy absorbed per unit time by each shell divided by the volume of the shell. We adopt the X-ray and UV spectrum from 0.1 to 280 nm estimated for GJ 832 as a representative M2 dwarf (Lloyd et al. 2016). The EUV flux at 1 au is taken to be  $1.1 \times 10^{-3} \text{ W m}^{-2}$ , which is about 0.25 times that from the present Sun. To represent both the higher EUV luminosity typical of young stars and a range of semi-major axes, we scale the stellar spectrum to consider EUV fluxes up to  $10^4$  times the Earth's level.

We consider radiative cooling by thermal line emission of  $\text{H}_2\text{O}$ ,  $\text{OH}$ ,  $\text{H}_3^+$ ,  $\text{OH}^+$ , and  $\text{H}_3\text{O}^+$ . The radiative cooling rate due to a transition from energy level  $i$  to  $j$  of radiatively active molecular species  $s$  is given by

$$q_{\text{rad},s,ij} = n_{s,i} A_{ij} h\nu_{ij} \beta_{ij}, \quad (\text{D.12})$$

where  $n_{s,i}$  is the population density in level  $i$ ,  $A_{ij}$  is the spontaneous transition probability,  $h\nu_{ij}$  is the energy difference between level  $i$  and level  $j$ , and  $\beta_{ij}$  is the photon escape probability. The total radiative cooling rate by species  $s$  is calculated by summing the radiative cooling rates of all the transitions. The population density  $n_{s,i}$  is calculated under the assumption of local thermodynamic equilibrium as

$$n_{s,i} = n_s \frac{g_i}{Z} \exp\left(-\frac{E_i}{k_B T}\right) \quad (\text{D.13})$$

where  $n_s$  and  $Z$  are the total number density and partition function of species  $s$ , and  $g_i$  and  $E_i$  are the statistical weight and energy of level  $i$ . Approximating that half of the photons are emitted upward while the other half is emitted downward and then absorbed by dense, lower atmospheric layers, the bulk escape probability is evaluated by

$$\beta_{ij}(r) = \frac{1}{2} \int_0^\infty \phi(\nu, r) \exp\left[-\int_{r_{\text{top}}}^r \alpha_{L,ij} \phi(\nu, r) dr\right] d\nu \quad (\text{D.14})$$

where  $r_{\text{top}}$  is the radius of the outer boundary (the top of the atmosphere),  $\alpha_{L,ij}$  is the absorption coefficient integrated over frequency, and  $\phi(\nu, r)$  is the line profile,  $\alpha_{L,ij}$  is given by

$$\alpha_{L,ij} = \frac{c^2}{8\pi\nu_{ij}^2} n_{s,i} A_{ij} \left( \frac{n_{s,j} g_i}{n_{s,i} g_j} - 1 \right). \quad (\text{D.15})$$

Assuming a Doppler-broadened line profile,  $\phi(\nu, r)$  is given by

$$\phi(\nu, r) = \frac{1}{\sqrt{\pi} \Delta\nu_D} \exp\left[-\frac{1}{(\Delta\nu_D)^2} \left(\nu - \nu_0 - \frac{u_s(r)}{c} \nu_0\right)^2\right], \quad (\text{D.16})$$

where  $u_s(r)$  is the velocity profile of radiative sources and  $\nu_0$  is the rest-frame central frequency of the line profile; and  $\Delta\nu_D$  is the Doppler width given by

$$\Delta\nu_D = \frac{\nu_0}{c} \sqrt{\frac{3k_B T}{m_s}}, \quad (\text{D.17})$$

where  $m_s$  is the molecular mass of species  $s$ . The net radiative cooling rate  $q_{\text{rad}}$  is obtained by the sum of contributions by  $\text{H}_2\text{O}$ ,  $\text{OH}$ ,  $\text{H}_3^+$ , and  $\text{OH}^+$ . We use the line data provided by the HITRAN database (Rothman et al. 2013; <http://hitran.org>) and ExoMol database (Tennyson et al. 2016; <http://exomol.com>).

We consider 31,333 transitions of  $\text{H}_2\text{O}$  and 4043 transitions of  $\text{OH}$  to cover over 99% of total energy emission within the 100–3000 K temperature range. The emission from  $\text{H}_3^+$ ,  $\text{OH}^+$ , and  $\text{H}_3\text{O}^+$  are assumed to be optically thin throughout the flow, with all lines from the ExoMol database (Tennyson et al. 2016).

#### D.4. Calculation method

The governing equations are solved by numerical time integration until the physical quantities reach their steady-state profiles. These equations can be split into advection phases and non-advection phases. We employ the CIP method to solve for the advection phases (Yabe & Aoki 1991) to achieve numerical stability and accuracy for hydrodynamic escape simulations (Kuramoto et al. 2013). After solving the advection phases, we solve the non-advection phases with a finite-difference approach. The non-advection phases of the energy equation are solved explicitly. Those of the continuity equations are solved with the semi-implicit method. Those of the momentum equations are solved implicitly using the quantities for the next time step that are obtained by the integration of the energy equation and the continuity equations.

1000 spatial grids in radial coordinates are taken with the grid-to-grid intervals exponentially increasing with  $r$ . The time step is defined so as to satisfy the CFL condition. For each parameter setup, we continue the time integration until reaching the steady state using the convergence condition described in Tian et al. (2005).

The lower and upper boundaries are set to  $r = R_p, 50R_p$ , respectively, where  $R_p$  is the radius of the planet. In each simulation run, the atmospheric density and temperature at the lower boundary are fixed. We assume that only  $\text{H}_2$  and  $\text{H}_2\text{O}$  exist at the lower boundary. The number density of  $\text{H}_2$  at the lower boundary is set to  $1 \times 10^{19} \text{ m}^{-3}$ . The number density of  $\text{H}_2\text{O}$  is given as a parameter in each simulation run. The temperature at the lower boundary is set to 400 K. This corresponds to the skin temperature, the asymptotic temperature at high altitudes of the upper atmosphere that is optically thin in the thermal-IR and transparent to shortwave radiation (Catling & Kasting 2017). The other physical quantities at the lower and upper boundaries are estimated by linear extrapolations from the calculated domain. As the initial condition, we use the steady-state profiles of the pure  $\text{H}_2$  atmosphere and add  $\text{H}_2\text{O}$  whose number density profiles are given by the hydrostatic structure. The initial velocity of  $\text{H}_2\text{O}$  is set at  $1 \times 10^{-5} \text{ m s}^{-1}$ .

## Appendix E: Water abundance in the upper atmosphere

Even if the lower atmosphere contains plentiful  $\text{H}_2\text{O}$  (as steam), the abundance in the upper atmosphere can be ultimately limited by the saturation vapor pressure where it is lowest relative to the total local pressure. Figure E.1 plots a schematic radiative-convective (R-C) atmosphere where the upper radiative zone is uniformly at the skin temperature  $T_{\text{eq}}/2^{0.25}$  (here set to the Earth-like value of 255 K), and the convective zone is an adiabat with  $\gamma = 1.4$ , appropriate for  $\text{H}_2$ . The R-C boundary (circle) is set at 0.1 bar, a value which is typical for Solar System atmospheres (Robinson & Catling 2012). Curves of the saturation vapor-pressure over ice or liquid  $\text{H}_2\text{O}$  (Bohren & Albrecht 1998), scaled for different mixing ratios, are plotted. Water vapor in rising atmospheric parcels will condense out and form clouds

Table D.1: Chemical reactions included in the model

No.	Reaction		Reaction rate $\text{cm}^3 \text{s}^{-1}$
R1	$\text{H}_2 + h\nu$	$\rightarrow \text{H} + \text{H}$	
R2		$\rightarrow \text{H}_2^+ + \text{e}$	
R3		$\rightarrow \text{H}^+ + \text{H} + \text{e}$	
R4	$\text{H}_2\text{O} + h\nu$	$\rightarrow \text{H} + \text{OH}$	
R5		$\rightarrow \text{H}_2 + \text{O}(^1\text{D})$	
R6		$\rightarrow \text{O} + \text{H} + \text{H}$	
R7		$\rightarrow \text{OH}^+ + \text{H} + \text{e}$	
R8		$\rightarrow \text{O}^+ + \text{H}_2 + \text{e}$	
R9		$\rightarrow \text{H}^+ + \text{OH} + \text{e}$	
R10		$\rightarrow \text{H}_2\text{O}^+ + \text{e}$	
R11	$\text{H} + h\nu$	$\rightarrow \text{H}^+ + \text{e}$	
R12	$\text{O} + h\nu$	$\rightarrow \text{O}^+ + \text{e}$	
R13	$\text{OH} + h\nu$	$\rightarrow \text{O} + \text{H}$	
R14		$\rightarrow \text{OH}^+ + \text{e}$	
R15		$\rightarrow \text{O}(^1\text{D}) + \text{H}$	
R16	$\text{O}_2 + h\nu$	$\rightarrow \text{O} + \text{O}$	
R17		$\rightarrow \text{O} + \text{O}(^1\text{D})$	
R18		$\rightarrow \text{O}^+ + \text{O} + \text{e}$	
R19		$\rightarrow \text{O}_2^+ + \text{e}$	
R20	$\text{H}_2 + \text{H}_2$	$\rightarrow \text{H}_2 + \text{H} + \text{H}$	$1.0 \times 10^{-8} \exp(-84000/T)$
R21	$\text{H}_2 + \text{H}_2\text{O}$	$\rightarrow \text{OH} + \text{H}_2 + \text{H}$	$5.8 \times 10^{-9} \exp(-52900/T)$
R22	$\text{H}_2 + \text{O}_2$	$\rightarrow \text{O} + \text{O} + \text{H}_2$	$6.0 \times 10^{-9} \exp(-52300/T)$
R23	$\text{H}_2 + \text{O}_2$	$\rightarrow \text{OH} + \text{OH}$	$3.16 \times 10^{-10} \exp(-21890/T)$
R24	$\text{H}_2 + \text{OH}$	$\rightarrow \text{O} + \text{H}_2 + \text{H}$	$6.0 \times 10^{-9} \exp(-50900/T)$
R25	$\text{H}_2 + \text{H}$	$\rightarrow \text{H} + \text{H} + \text{H}$	$4.67 \times 10^{-7} (T/300)^{-1} \exp(-55000/T)$
R26	$\text{H}_2 + \text{H}_2^+$	$\rightarrow \text{H}_3^+ + \text{H}$	$2.08 \times 10^{-9}$
R27	$\text{H}_2 + \text{H}_2\text{O}^+$	$\rightarrow \text{H}_3\text{O}^+ + \text{H}$	$6.40 \times 10^{-10}$
R28	$\text{H}_2 + \text{O}^+$	$\rightarrow \text{OH}^+ + \text{H}$	$1.70 \times 10^{-9}$
R29	$\text{H}_2 + \text{OH}^+$	$\rightarrow \text{H}_2\text{O}^+ + \text{H}$	$1.01 \times 10^{-9}$
R30	$\text{H}_2 + \text{O}$	$\rightarrow \text{OH} + \text{H}$	$3.14 \times 10^{-13} (T/300)^{2.7} \exp(-3150/T)$
R31	$\text{H}_2 + \text{OH}$	$\rightarrow \text{H}_2\text{O} + \text{H}$	$2.05 \times 10^{-12} (T/300)^{1.52} \exp(-1736/T)$
R32	$\text{H}_2 + \text{O}(^1\text{D})$	$\rightarrow \text{H} + \text{OH}$	$1.0 \times 10^{-9}$
R33	$\text{H}_2\text{O} + \text{H}$	$\rightarrow \text{OH} + \text{H} + \text{H}$	$5.80 \times 10^{-9} \exp(-52900/T)$
R34	$\text{H}_2\text{O} + \text{H}^+$	$\rightarrow \text{H}_2\text{O}^+ + \text{H}$	$6.90 \times 10^{-9} (T/300)^{-0.5}$
R35	$\text{H}_2\text{O} + \text{H}_2^+$	$\rightarrow \text{H}_2\text{O}^+ + \text{H}_2$	$3.90 \times 10^{-9} (T/300)^{-0.5}$
R36	$\text{H}_2\text{O} + \text{O}^+$	$\rightarrow \text{H}_2\text{O}^+ + \text{O}$	$3.20 \times 10^{-9} (T/300)^{-0.5}$
R37	$\text{H}_2\text{O} + \text{OH}^+$	$\rightarrow \text{H}_2\text{O}^+ + \text{OH}$	$1.59 \times 10^{-9} (T/300)^{-0.5}$
R38	$\text{H}_2\text{O} + \text{H}_2^+$	$\rightarrow \text{H}_3\text{O}^+ + \text{H}$	$3.40 \times 10^{-9} (T/300)^{-0.5}$
R39	$\text{H}_2\text{O} + \text{H}_2\text{O}^+$	$\rightarrow \text{H}_3\text{O}^+ + \text{OH}$	$2.10 \times 10^{-9} (T/300)^{-0.5}$
R40	$\text{H}_2\text{O} + \text{H}_3^+$	$\rightarrow \text{H}_3\text{O}^+ + \text{H}_2$	$5.90 \times 10^{-9} (T/300)^{-0.5}$
R41	$\text{H}_2\text{O} + \text{OH}^+$	$\rightarrow \text{H}_3\text{O}^+ + \text{O}$	$1.30 \times 10^{-9} (T/300)^{-0.5}$
R42	$\text{H}_2\text{O} + \text{H}$	$\rightarrow \text{OH} + \text{H}_2$	$1.59 \times 10^{-11} (T/300)^{1.2} \exp(-9600/T)$
R43	$\text{H}_2\text{O} + \text{O}$	$\rightarrow \text{OH} + \text{OH}$	$1.85 \times 10^{-11} (T/300)^{0.95} \exp(-8571/T)$
R44	$\text{H} + \text{OH}$	$\rightarrow \text{O} + \text{H} + \text{H}$	$6.00 \times 10^{-9} \exp(-50900/T)$
R45	$\text{H} + \text{H}_2^+$	$\rightarrow \text{H}_2 + \text{H}^+$	$6.40 \times 10^{-10}$
R46	$\text{H} + \text{O}^+$	$\rightarrow \text{O} + \text{H}^+$	$5.66 \times 10^{-10} (T/300)^{0.36} \exp(8.6/T)$
R47	$\text{H} + \text{H}^+$	$\rightarrow \text{H}_2^+$	$1.15 \times 10^{-18} (T/300)^{1.49} \exp(-228/T)$
R48	$\text{H} + \text{O}_2$	$\rightarrow \text{O} + \text{O} + \text{H}$	$6.0 \times 10^{-9} \exp(-52300/T)$
R49	$\text{H} + \text{O}_2$	$\rightarrow \text{OH} + \text{O}$	$2.61 \times 10^{-10} \exp(-8156/T)$
R50	$\text{H} + \text{O}$	$\rightarrow \text{OH}$	$9.90 \times 10^{-19} (T/300)^{-0.38}$

Ref. McElroy et al. (2013)

up to a maximum altitude at the R-C boundary where the vapor pressure is lowest. The  $\text{H}_2\text{O}/\text{H}_2$  ratio at that boundary and higher altitudes is then set by the saturation vapor pressure curve that intersects the R-C boundary point (in this case,  $1.3 \times 10^{-4}$ ). Lower or higher  $T_{\text{eq}}$  results in lower or higher  $\text{H}_2\text{O}/\text{H}_2$ , accordingly, and this variation describes the curve in Fig. 3. (The curve

is not sensitive to the exact location of the R-C boundary). that the turbopause, above which molecular diffusion dominates over eddy diffusion, is predicted to lie at  $\sim 10^{-4}$  bar, well above the plot.

Table D.2: Chemical reactions (continued)

No.	Reaction	Reaction rate $\text{cm}^3 \text{s}^{-1}$
R51	$\text{H} + \text{OH} \rightarrow \text{H}_2\text{O}$	$5.26 \times 10^{-18} (T/300)^{-5.22} \exp(-90/T)$
R52	$\text{H} + \text{OH} \rightarrow \text{O} + \text{H}_2$	$6.99 \times 10^{-14} (T/300)^{2.8} \exp(-1950/T)$
R53	$\text{O} + \text{H}^+ \rightarrow \text{O}^+ + \text{H}$	$6.86 \times 10^{-10} (T/300)^{0.26} \exp(-224.3/T)$
R54	$\text{O} + \text{H}_2^+ \rightarrow \text{OH}^+ + \text{H}$	$1.50 \times 10^{-9}$
R55	$\text{O} + \text{H}_3^+ \rightarrow \text{H}_2\text{O}^+ + \text{H}$	$3.42 \times 10^{-10} (T/300)^{-0.16} \exp(-1.4/T)$
R56	$\text{O} + \text{H}_3^+ \rightarrow \text{OH}^+ + \text{H}_2$	$7.98 \times 10^{-10} (T/300)^{-0.16} \exp(-1.4/T)$
R57	$\text{O} + \text{H}_2\text{O}^+ \rightarrow \text{O}_2^+ + \text{H}_2$	$4.0 \times 10^{-11}$
R58	$\text{O} + \text{OH}^+ \rightarrow \text{O}_2^+ + \text{H}$	$7.10 \times 10^{-10}$
R59	$\text{O} + \text{OH} \rightarrow \text{O}_2 + \text{H}$	$3.69 \times 10^{-11} (T/300)^{-0.27} \exp(-12.9/T)$
R60	$\text{O} + \text{O} \rightarrow \text{O}_2$	$4.9 \times 10^{-20} (T/300)^{1.58}$
R61	$\text{O}(^1\text{D}) \rightarrow \text{O}$	$1.0 \times 10^{-4}$
R62	$\text{O}(^1\text{D}) + \text{H}_2\text{O} \rightarrow \text{OH} + \text{OH}$	$2.2 \times 10^{-9}$
R63	$\text{O}(^1\text{D}) + \text{H}_2 \rightarrow \text{H} + \text{OH}$	$1.0 \times 10^{-9}$
R64	$\text{O}(^1\text{D}) + \text{O}_2 \rightarrow \text{O}_2 + \text{O}$	$3.2 \times 10^{-11} \exp(70/T)$
R65	$\text{O}(^1\text{D}) + \text{O} \rightarrow \text{O} + \text{O}$	$8.0 \times 10^{-12}$
R66	$\text{OH} + \text{H}^+ \rightarrow \text{OH}^+ + \text{H}$	$2.1 \times 10^{-9} (T/300)^{-0.5}$
R67	$\text{OH} + \text{H}_2^+ \rightarrow \text{OH}^+ + \text{H}_2$	$7.6 \times 10^{-10} (T/300)^{-0.5}$
R68	$\text{OH} + \text{O}^+ \rightarrow \text{OH}^+ + \text{O}$	$3.6 \times 10^{-10} (T/300)^{-0.5}$
R69	$\text{OH} + \text{H}_2^+ \rightarrow \text{H}_2\text{O}^+ + \text{H}$	$7.6 \times 10^{-10} (T/300)^{-0.5}$
R70	$\text{OH} + \text{H}_3^+ \rightarrow \text{H}_2\text{O}^+ + \text{H}_2$	$1.3 \times 10^{-9} (T/300)^{-0.5}$
R71	$\text{OH} + \text{O}^+ \rightarrow \text{O}_2^+ + \text{H}$	$3.6 \times 10^{-10} (T/300)^{-0.5}$
R72	$\text{OH} + \text{OH}^+ \rightarrow \text{H}_2\text{O}^+ + \text{O}$	$7.0 \times 10^{-10} (T/300)^{-0.5}$
R73	$\text{OH} + \text{H}_2\text{O}^+ \rightarrow \text{H}_3\text{O}^+ + \text{O}$	$6.9 \times 10^{-10} (T/300)^{-0.5}$
R74	$\text{OH} + \text{OH} \rightarrow \text{H}_2\text{O} + \text{O}$	$1.65 \times 10^{-12} (T/300)^{1.14} \exp(-50/T)$
R75	$\text{O}_2 + \text{H}^+ \rightarrow \text{O}_2^+ + \text{H}$	$2.0 \times 10^{-9}$
R76	$\text{O}_2 + \text{H}_2^+ \rightarrow \text{O}_2^+ + \text{H}_2$	$8.0 \times 10^{-10}$
R77	$\text{O}_2 + \text{H}_2\text{O}^+ \rightarrow \text{O}_2^+ + \text{H}_2\text{O}$	$4.6 \times 10^{-10}$
R78	$\text{O}_2 + \text{O}^+ \rightarrow \text{O}_2^+ + \text{O}$	$1.9 \times 10^{-11}$
R79	$\text{O}_2 + \text{OH}^+ \rightarrow \text{O}_2^+ + \text{OH}$	$5.9 \times 10^{-10}$
R80	$\text{H}^+ + e \rightarrow \text{H} + \text{PHOTON}$	$3.5 \times 10^{-12} (T/300)^{-0.75}$
R81	$\text{H}_2^+ + e \rightarrow \text{H} + \text{H}$	$1.6 \times 10^{-8} (T/300)^{-0.43}$
R82	$\text{H}_3^+ + e \rightarrow \text{H}_2 + \text{H}$	$2.34 \times 10^{-8} (T/300)^{-0.52}$
R83	$\text{H}_3^+ + e \rightarrow \text{H} + \text{H} + \text{H}$	$4.36 \times 10^{-8} (T/300)^{-0.52}$
R84	$\text{O}^+ + e \rightarrow \text{O} + \text{PHOTON}$	$3.24 \times 10^{-12} (T/300)^{-0.66}$
R85	$\text{O}_2^+ + e \rightarrow \text{O} + \text{O}$	$1.95 \times 10^{-7} (T/300)^{-0.7}$
R86	$\text{OH}^+ + e \rightarrow \text{O} + \text{H}$	$3.75 \times 10^{-8} (T/300)^{-0.5}$
R87	$\text{H}_2\text{O}^+ + e \rightarrow \text{O} + \text{H}_2$	$3.9 \times 10^{-8} (T/300)^{-0.5}$
R88	$\text{H}_2\text{O}^+ + e \rightarrow \text{O} + \text{H} + \text{H}$	$3.05 \times 10^{-7} (T/300)^{-0.5}$
R89	$\text{H}_2\text{O}^+ + e \rightarrow \text{OH} + \text{H}$	$8.6 \times 10^{-8} (T/300)^{-0.5}$
R90	$\text{H}_3\text{O}^+ + e \rightarrow \text{H}_2\text{O} + \text{H}$	$7.09 \times 10^{-8} (T/300)^{-0.5}$
R91	$\text{H}_3\text{O}^+ + e \rightarrow \text{O} + \text{H}_2 + \text{H}$	$5.60 \times 10^{-9} (T/300)^{-0.5}$
R92	$\text{H}_3\text{O}^+ + e \rightarrow \text{OH} + \text{H}_2$	$5.37 \times 10^{-8} (T/300)^{-0.5}$
R93	$\text{H}_3\text{O}^+ + e \rightarrow \text{OH} + \text{H} + \text{H}$	$3.05 \times 10^{-7} (T/300)^{-0.5}$

Ref. McElroy et al. (2013)

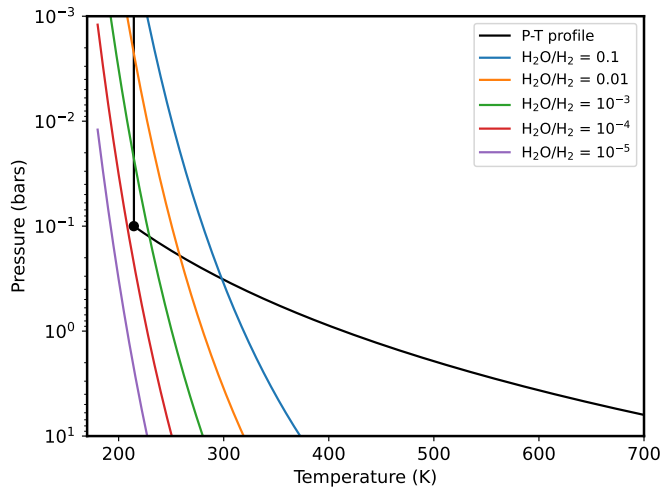


Fig. E.1: Pressure-temperature profile (black curve) in a simplified  $H_2$ -rich atmosphere with a radiative-convective boundary at 0.1 bar pressure (black point). The colored lines represent the vapor pressures for different  $H_2O/H_2$  mixing ratios, and the lowest vapor pressure along the profile occurs at the R-C boundary (black filled circle).